Journal of Colloid and Interface Science 670 (2024) 204–214

Contents lists available at ScienceDirect

Journal of Colloid And Interface Science

journal homepage: www.elsevier.com/locate/jcis

Regular Article

Enhanced stability and kinetic performance of sandwich Si anode constructed by carbon nanotube and silicon carbide for lithium-ion battery

Fang Di [a], Xin Gu [a,c], Yang Chu [a], Lixiang Li [a,*], Xin Geng [a], Chengguo Sun [a], Weimin Zhou [a], Han Zhang [a], Hongwei Zhao [a], Lin Tao [a], Guangshen Jiang [a], Xueyuan Zhang [b], Baigang An [a,b,*]

[a] Key Laboratory of Energy Materials and Electrochemistry Liaoning Province, School of Chemical Engineering, University of Science and Technology Liaoning, 185 Qianshanzhong Road, Anshan 114051, Liaoning, China
[b] Institute of Corrosion Science and Technology, 136 Kaiyuan Road, Guangzhou 510530, Guangdong, China
[c] Liaoning Light Industry Institute Co., Ltd., 46 Taishan Road, Shenyang 110031, Liaoning, China

GRAPHICAL ABSTRACT

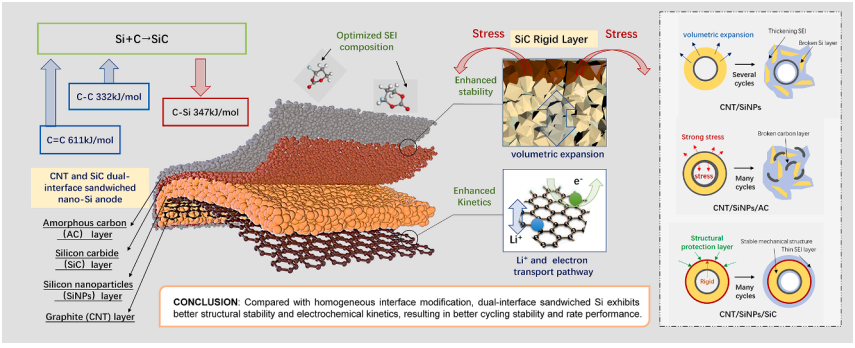

ARTICLE INFO

Keywords:
Interface engineering
Si anode
Stress-buffer
Kinetic performance
Axial structure

ABSTRACT

Owing to highly theoretical capacity of 3579 mAh/g for lithium-ion storage at ambient temperature, silicon (Si) becomes a promising anode material of high-performance lithium-ion batteries (LIBs). However, the large volume change (~300 %) during lithiation/delithiation and low conductivity of Si are challenging the commercial developments of LIBs with Si anode. Herein, a sandwich structure anode that Si nanoparticles sandwiched between carbon nanotube (CNT) and silicon carbide (SiC) has been successfully constructed by acetylene chemical vapor deposition and magnesiothermic reduction reaction technology. The SiC acts as a stiff layer to inhibit the volumetric stress from Si and the inner graphited CNT plays as the matrix to cushion the volumetric stress and as the conductor to transfer electrons. Moreover, the combination of SiC and CNT can relax the surface stress of carbonaceous interface to synergistically prevent the integrated structure from the degradation to avoid the solid electrolyte interface (SEI) reorganization. In addition, the SiC (111) surface has a strong ability to adsorb fluoroethylene carbonate molecule to further stabilize the SEI. Consequently, the CNT/SiNPs/SiC anode can stably supply the capacity of 1127.2 mAh/g at 0.5 A/g with a 95.6 % capacity retention rate after 200 cycles and an excellent rate capability of 745.5 mAh/g at 4.0 A/g and 85.5 % capacity retention rate after 1000 cycles. The

* Corresponding authors at: Key Laboratory of Energy Materials and Electrochemistry Liaoning Province, School of Chemical Engineering, University of Science and Technology Liaoning, 185 Qianshanzhong Road, Anshan 114051, Liaoning, China (B. An).
E-mail addresses: lxli2005@126.com (L. Li), bgan@ustl.edu.cn (B. An).

https://doi.org/10.1016/j.jcis.2024.05.081
Received 8 January 2024; Received in revised form 11 May 2024; Accepted 13 May 2024
Available online 15 May 2024

present study could give a guide to develop the functional Si anode through designing a multi-interface with heterostructures.

1. Introduction

The development of rechargeable lithium-ion batteries (LIBs) in electric vehicle power systems and smart storage stations for intermittent renewable energy is contingent upon the availability of electrode materials with high capacity. [1–3] Silicon (Si) is regarded as a highly promising anode for replacing graphite, given its considerable theoretical capacity of 3579 mAh/g, appropriate discharge potentials (0.4 V vs Li^+/Li) and natural abundance [4,5]. Nevertheless, the low conductivity of Si impedes the kinetics of (de)lithiation processes [6], and the considerable volume change (~300 %) during (de)lithiation results in the pulverisation of the anode and the repeated formation of a solid electrolyte interface (SEI) film around Si particles, thereby rendering the advantages of Si anode difficult to exploit.

Numerous studies have demonstrated that the combination of Si nanoparticles (SiNPs) with carbonaceous materials with good conductivity can enhance the kinetics and stability of the anode [7]. Amorphous carbon and heteroatom-doped carbons have been widely employed to mitigate mechanical failures, prevent direct contact between the Si surface and the electrolyte, and facilitate the formation of conductive pathways [8–10]. However, they are not sufficiently robust to withstand the significant volumetric stress induced by Si lithiation (Fig. S1a) [11,12]. Constructing the free volume through a Si-carbon structure is an effective strategy to accommodate the volume expansion, such as yolk-shell or wire-in-tube structures [13–16]. However, the formation of such free space may result in the contact of Si particles with the conductive carbon phase by a few points, which could slow the charge transport between the Si and the current collector (Fig. S1b and c) [17,18]. To enhance the mechanical stability of the Si anode, inert materials such as SiO_2, TiO_2 and SiC with high mechanical strength have been employed to mitigate the volumetric stress resulting from Si lithiation [19–21]. However, an inert surface layer generally impedes the transport of Li^+ and electrons, thus reducing the rate capability of LIBs (Fig. S1d) [22].

Although SEI film allows Li^+ transport, the repeated formation of SEI film can deplete more electrolytes and increase the transport distance of electrons and ions [23,24]. The interface chemistry between the electrode and the electrolyte plays an important role on the SEI properties. The active film-forming species in electrolytes generally act as additives to modify the physical, chemical and mechanical properties of the SEI, thereby increasing the interface stability between the active materials and the electrolyte. For example, fluoroethylene carbonate (FEC), which is the most common electrolyte additive for Si-based anodes, can promote the passivation of the electrode/electrolyte interface and optimise the SEI composition [25]. Nevertheless, the prerequisite for their participation in the formation of the SEI is the preferential adsorption of the FEC additive on the electrode surface [26,27].

Herein, a novel Si-based anode comprising CNT/SiNPs/SiC has been constructed by acetylene chemical vapor deposition (CVD) and magnesiothermic reduction reaction (MRR) technology. The material features a carbon nanotube (CNT) and silicon carbide (SiC) dual-interface sandwiched SiNPs. The inner CNT can act as a conductor to facilitate the transfer of electrons and a buffer to mitigate volumetric stress resulting from Si lithiation. The stiff SiC interfaced with SiNPs can inhibit substantial structure inflation and relax the stress on the inner CNT, thereby preventing structural failure (Scheme 1 illustrates the preparation, structure and working mechanism of CNT/SiNPs/SiC). Furthermore, the SiC (1 1 1) surface serves as an adsorption site for FEC molecules, thereby further stabilising the SEI. Consequently, the CNT/SiNPs/SiC anode exhibits remarkable stability and satisfactory rate performance. After 1000 cycles at 4.0 A g^{-1}, it delivers a capacity of 745.5 mAh g^{-1}, with an 85.5 % capacity retention rate.

2. Experimental

2.1. Chemicals and materials

Tetraethyl orthosilicate (TEOS) and Mg powder were purchased from the Aladdin Company. All other chemicals such as HNO_3, HCl, ammonia, ethanol solution were purchased from Sinopharm Chemical Reagent Company. HNO_3 and HCl solution are guaranteed reagent and other chemicals are analytical reagent.

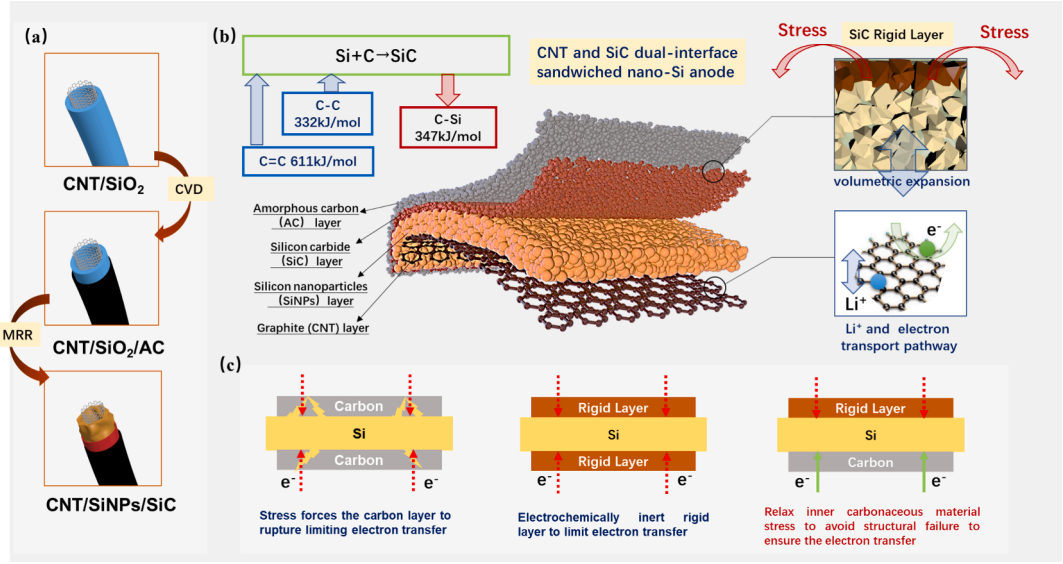

Scheme 1. Schematic illustration of CNT/SiNPs/SiC for (a) preparation process (b) material structure characteristics and (c) differences in electron transfer between homogeneous and heterogeneous interfaces.

2.2. Sample preparation

CNT/SiO_2. The CNTs were purified by using the concentrated HNO_3 (65–68 wt%) to remove amorphous carbons and then were used as the inner supports for the active Si materials. The purified CNTs were coated with the SiO_2 layer via the TEOS hydrolysis to prepare CNT/SiO_2 as the following process. The purified CNTs of 25.0 mg were dispersed in 200 mL ethanol containing 15 mL deionized water and 15 mL ammonia aqueous solution (25 wt%). After an ultrasonic dispersion of CNTs solution for 30 min, 3 mL TEOS/ethanol solution (10 vol%) was dropped into it. The resulted mixture was vigorously stirred for 6 h at room temperature and then was filtered and washed by deionized water. The finally filtered product was dried at 80 °C in a vacuum oven.

CNT/SiO_2/AC. The acetylene CVD technology was applied to deposit amorphous carbon layers around the CNT/SiO_2 to prepare CNT/SiO_2/AC as the following process. CNT/SiO_2 was placed in an argon atmosphere tube furnace and heated to 850 °C, after which the acetylene/argon mixture (10 vol%) was passed through furnace at a flow rate of 100 mL min^{-1} for 30 min.

CNT/SiNPs and CNT/SiNPs/SiC. The MRR was used to reduce the CNT/SiO_2 and CNT/SiO_2/AC into the CNT/SiNPs and CNT/SiNPs/SiC. Mg powders was mixed with SiO_2 as ratio of 4:5, and the mixture was heated to 650 °C at a ramp of 5 °C min^{-1} and the temperature was kept for 4 h under an argon atmosphere. After that, the furnace was cooled down to room temperature, the produced powders were immersed in 2.0 M HCl solution for 10 h to remove byproduct of MgO. The obtained CNT/SiNPs and CNT/SiNPs/SiC were washed by deionized water/alcohol and the filtered samples were dried at 80 °C under vacuum condition.

CNT/SiNPs/AC. In order to highlight the critical effects of SiC, as a counterpart, the CNT/SiNPs/AC was prepared by acetylene vapor deposition on CNT/SiNPs, the other parameters were consistent with CNT/SiNPs/SiC preparation process.

2.3. Materials characterization

The phase composition of samples was characterized by X-ray diffraction (XRD) (Rigaku X'pret Powder, D/MAX-2500X, Cu Kα). The microstructure and morphology of samples were observed by scanning electron microscope (SEM) (FEI Apreo, operated at 5 kV) and transmission electron microscope (TEM) (FEI Talos F200X, operated at 200 kV). The chemical states of materials were analyzed by X-ray photoelectron spectroscopy (XPS) (Axis Supra, Al Kα). The thermogravimetry of samples was performed by thermogravimetry (TG) analyzer (TA Instruments, TQ600) in pure air atmosphere. The physical adsorption-desoprtion isotherms of samples were measured by volumetric sorption analyzer (Micromeritics, ASAP2020). Pore size distribution (PSD) of materials was analyzed according to the nonlocal density functional theory (NLDFT) method.

2.4. Electrochemical tests

The anodes were fabricated by casting mixture of active material of CNT/SiNPs, CNT/SiNPs/AC or CNT/SiNPs/SiC, conductive carbon black (Super P) and carboxy methyl cellulose (CMC) with a weight ratio of 6:2:2 onto copper foil. The surface loading amount of the active material was about 0.5 mg cm^{-2}. The foils loaded with the active materials were dried at 70 °C in vacuum oven overnight and then punched to the disks with a diameter of 12 mm. Coin cells (2025type) were assembled in Ar-filled glove box. The CNT/SiNPs, CNT/SiNPs/AC or CNT/SiNPs/SiC electrode and a lithium metal disk were used as the working electrode and the counter/reference electrode. 1.0 M $LiPF_6$ dissolved in a mixture of ethylene carbonate (EC) and dimethyl carbonate (DMC) (1:1 in vol%) with 10 vol% FEC was used as the electrolyte. An electrochemical workstation (Gamry 3000) was used to test the cyclic voltammetry (CV) and electrochemical impedance spectroscopy (EIS). The cells were galvanostatically charged and discharged in the potential range of 0.01–1.5 V (vs. Li^+/Li) by an automatic battery tests system (LANHE CT3100). The galvanostatic intermittent titration technique (GITT) was used to measure the Li^+ diffusion rate of samples at 0.2 A/g with a pulse time of 20 min and a relaxation time of 30 min. Full-type cells were assembled to further evaluate the performance of CNT/SiNPs/SiC. The commercial $LiFePO_4$ (LFP) served as the cathode, and the pre-lithiated CNT/SiNPs/SiC electrode served as the anode. The pre-lithiation was enacted by discharging the above-mentioned half-cell at 0.2 A/g. Then the fully discharged cell was disassembled in a glove box to investigate the pre-lithiated CNT/SiNPs/SiC electrode. The capacity ratio of the negative electrode/positive electrode was 1.1, operating from 2.5 to 4.2 V.

2.5. Computational methods

Finite element model (FEM) were conducted by a thermalmechanical coupled model for stress distribution and the corresponding volumetric change evaluation of the experimental structure (the hoop surface displacements of all samples before and after fully lithiation as V_{LixSi}:V_{Si} = 3.8). According to the TEM images of sample, the model was built on the basis of 1/4 circular plane with the inner diameter of 40 nm, the outer diameter of 80 nm and an interface with 20 nm in thickness on both sides to simulate the material expansion process, and the axes of the circle are restricted to their radial displacements. The analysis of volume suppression and stress management depends on the material properties of multi-phase modification, such as the modulus of Young and the ratio of Poisson.

The first-principles calculations were carried out on the basis of density functional theory (DFT). To calculate the adsorption energy (Ead) of the FEC molecules on the Si (1 1 1) and SiC (1 1 1) surface, the following equation is described:

$$Eads = E(A/B) - E(A) - E(B)$$

where E(A/B), E(A) and E(B) are the overall energy of A and B after adsorption, the energy of adsorbate A, and the energy of adsorbent B, respectively.

3. Results and discussion

The impact of heterogeneous interfaces on diffusion-induced stress during the lithiation of Si-based anodes was validated through the utilisation of FEM. As illustrated in Fig. 1a and b, a dual-interface 1/4-cylinder model was constructed in accordance with previous work (Tab. S1) [28,29]. In contrast to the symmetric C//Si//C model, in which stress is uniformly distributed across both interfaces, the heterogeneous C//Si//SiC model concentrates stress on the SiC side following thermal expansion, while reducing stress on the internal carbon from 5.69 GPa to 2.09 GPa. The surface stress on the inner carbon layer of CNT is effectively buffered to ensure the long-term maintenance of the conductive networks of CNT/SiNPs/SiC. The rigid SiC interlayer enhanced the contact between the SiNPs and CNT, while simultaneously protecting the conductive interface for the electron transfer during the (de)lithiation of Si. This kind of stress management by the heterogeneous interface ensures the stability of the material structure and the conductive channels, thereby improving the cyclic stability and kinetic performance of CNT/SiNPs/SiC (Fig. 1c and d).

Both SEM and TEM were employed to observe the microstructure and morphological evolution process of the CNT/SiNPs/SiC. As illustrated in Fig. 2(a–d), the purified CNTs have an average diameter of approximately 40 nm. Following the deposition of SiO_2 and amorphous carbon, the CNTs assume a fibre-like morphology with a diameter of approximately 150 nm. The subsequent MRR process results in the formation of SiNPs and SiC, with the fibre-like morphology remaining intact but becoming rough due to the production of pores. From the TEM

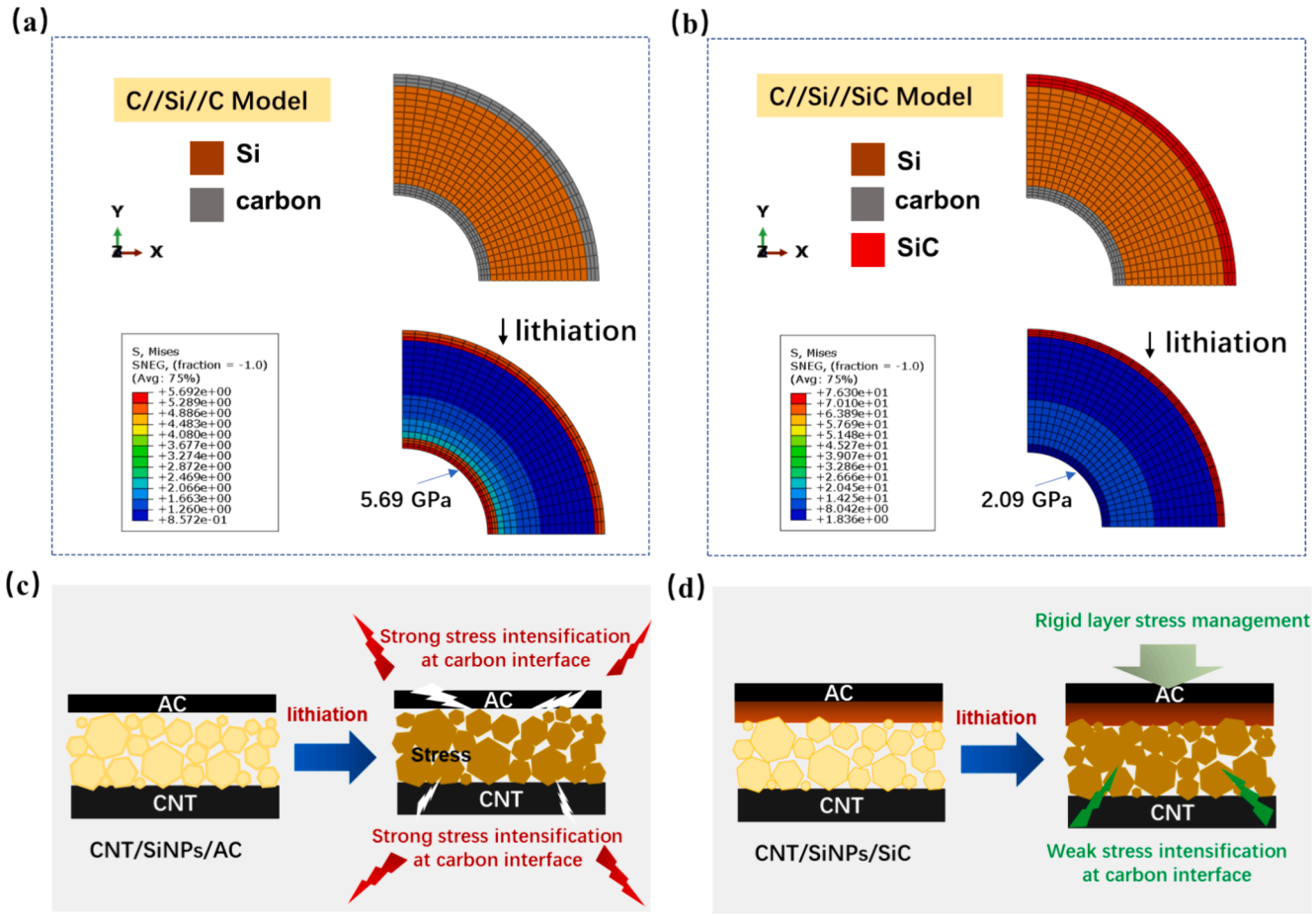

Fig. 1. Stress distribution of (a) C//Si//C and (b) C//Si//SiC models during the lithiation. (c) The schematic working principle of the homogenously dual-interfaces for AC and CNT and (d) the heterostructure dual-interface for SiC and CNT.

image of CNT/SiNPs/SiC, it is evident that the accumulated Si nanoparticles are present around the side wall of CNT (Fig. 2e). From high-resolution TEM images (Fig. 2f and g), it can be seen that the CNT with a highly graphitized wall can act as an effective inner conductor for electrochemical redox of SiNPs and a buffer to relieve volume stress. The lattice fringes of 0.31 nm and 0.25 nm indexing to the Si (1 1 1) and SiC (1 1 1) lattice planes can be identified, and the Si nanoparticles with a size of approximately 8.0 nm can be observed in Fig. 2g [30]. The production processes of Si nanoparticles can be deduced from Fig. S2-S4. The CNT/SiO_2 appears to have a dense surface due to the abundance of oxygen-containing groups on the CNT, which results in the homogeneous encapsulation of SiO_2 around the CNTs. After MRR, the CNT/SiO_2 is converted into CNT/SiNPs with a rough surface, which is attributed to the density difference between SiO_2 and Si, which produces many pores. Furthermore, the incorporation of the SiNPs with a size of less than 150 nm has been demonstrated to reduce the volumetric stress, thereby mitigating the risk of mechanical failure of the anode [31,32]. The selected area electronic diffraction (SAED) of the (1 1 1), (2 2 0), and (3 1 1) crystal planes of cubic Si (Fig. 2h) provides additional evidence for the uniform distribution of Si particles. The elemental mapping of CNT/SiNPs/SiC (Fig. 2i) reveals that the Si nanoclusters are densely distributed around the tubular CNT, while the carbon elements are concentrated in the central axes and the shells that sandwich the SiNPs. The oxygen elements are uniformly distributed along the overall framework of sample due to oxygen species containing in the CNT and the amorphous carbon layers.

The phase composition of the samples was examined by XRD, and the results are shown in Fig. 3a. The presence of graphitic and amorphous carbon, as well as SiO_2, nanocrystalline Si and SiC, can be distinguished by the characteristic peaks observed. This indicates that the MRR process results in the amorphous SiO_2 layer being converted into polycrystalline Si (Eq. (1)), further reacts with amorphous carbon rather than CNT to form SiC [33,34]. As shown in Eq. (2), the interfacial reaction between the SiO_2 layer and the amorphous carbon layer produces SiC in the exothermic influence of MRR. As a contrast sample, the MRR on the CNT/SiNPs was performed, there are no SiC formation, since the graphitic walls of CNT requires the higher energy than amorphous carbon to form SiC (Fig. S5). Furthermore, the XRD pattern of the MRR on CNT/SiNPs/AC (Fig. S6) excludes the possibility that Si reacted with amorphous carbon to produce SiC during CVD. This is because the temperature of Si reacting with carbon to produce SiC is above 1400 °C [35].

$$SiO_2 + 2Mg \rightarrow Si + 2MgO \quad (1)$$

$$Si + C \rightarrow SiC \quad (2)$$

The interactions between the individual components of CNT/SiNPs/SiC are of particular importance for the stability of the Si-based anode. XPS was employed to elucidate these interactions. The peaks with binding energies of 101.3, 152.3, 284.3 and 531.4 eV correspond to Si 2p, Si 2s, C 1s and O 1s, respectively, as illustrated in Fig. S7. Fig. 3c displays the high-resolution XPS spectrum of the Si 2p, which shows a strong Si-Si peak at a binding energy of 100.2 eV, a Si-C peak at 102.2 eV, and a weak Si-O peak at 103.5 eV, respectively. Furthermore, the deconvolution spectra of C1s (Fig. 3d) were performed. The presence of an additional peak in CNT/SiNPs/SiC at a binding energy of 282.4 eV is attributed to the C-Si bonding in the SiC layer [36,37].

The TG measurements were employed to analyse the composition

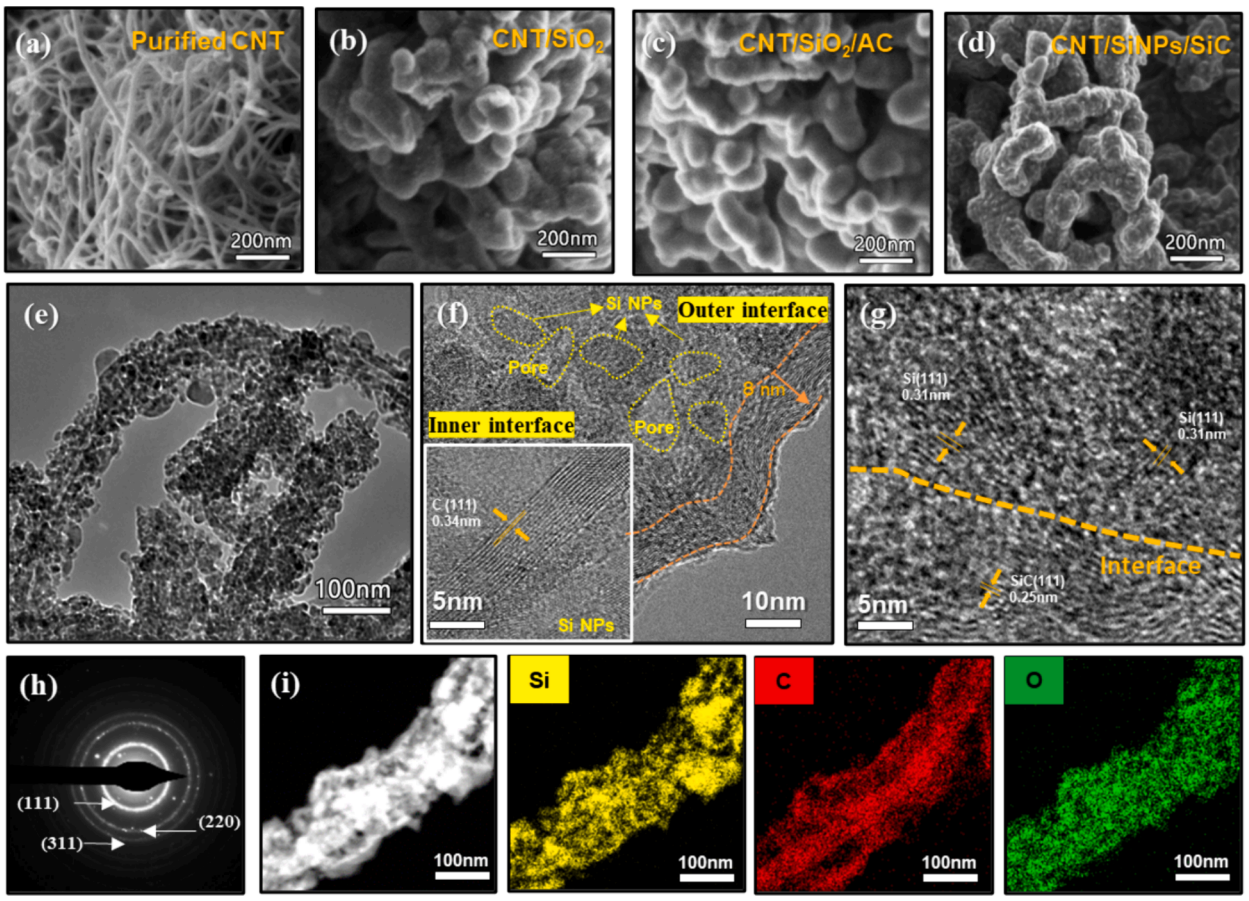

Fig. 2. SEM images of samples (a) Purified CNT, (b) CNT/SiO_2, (c) CNT/SiO_2/AC, (d) CNT/SiNPs/SiC. (e) TEM images of CNT/SiNPs/SiC. (f) TEM images of inner and outer interfaces of CNT/SiNPs/SiC. (g) HRTEM images of CNT/SiNPs/SiC. (h) SAED pattern with the diffraction rings indexed. (i) Corresponding element mapping of Si, C, and O in CNT/SiNPs/SiC.

and contents of the samples. As illustrated in Fig. 3e, a pronounced decline in weight is observed at approximately 550–620 °C for all samples, which can be attributed to the combustion of carbon fractions. The weight loss temperature of CNT/SiO_2/AC (550 °C) is slightly lower than that of CNT/SiO_2 (580 °C), due to the lower combustion temperature of the amorphous layers produced by acetylene CVD. It can be observed that the weight begins to decrease for CNT/SiNPs/SiC at approximately 620 °C. This could be attributed to the highly graphitised degree of carbon by MRR at 650 °C, which results in an increase in the combustion temperature. A weight gain of CNT/SiNPs/SiC at 730 °C can be attributed to the oxidation of Si, given that both SiC and SiO_2 exhibit good thermal stability at this temperature [38]. The heat flow curves of CNT/SiO_2 and CNT/SiO_2/AC (Fig. S8) can be used to calculate the content of SiO_2, CNT and amorphous carbon. Furthermore, the content of Si and SiC in CNT/SiNPs/SiC can be calculated and analysed according to the Eqs. (1) and (2), given that the SiC is derived from the reaction of Si with the amorphous carbon (Fig. 3f).

The porosity of materials is a crucial factor in determining the accessibility of active sites and facilitating ion transport. As illustrated in Fig. 3g, all samples exhibit the typical type IV isotherms, indicating a mesoporous and microporous structure with pore sizes ranging from 5 to 100 nm (Fig. S9 and Tab. S2) [39]. The conversion of SiO_2 into Si results in the formation of numerous pores due to the difference in the densities. In comparison to CNT/SiNPs, CNT/SiNPs/SiC contains a greater number of mesopores with a size range of approximately 5–10 nm. This can be attributed to the domain-limiting effect of the rigid SiC, as illustrated in Fig. 3b. The hierarchical pores of CNT/SiNP/SiC are beneficial in mitigating the volumetric expansion during Si lithiation and storing the electrolyte to facilitate ion transport, thereby enhancing the durability and rate performance of the Si-based anode.

The effects of composition and structure of samples on the electrochemical performance of Si-based anodes of LIBs were evaluated. The anode comprising CNT/SiNPs/SiC exhibited a high specific capacity of 1127.3 mAh/g at 0.5 A/g after 200 cycles, corresponding to a remarkable capacity retention of 95.6 % (Fig. 4a and Fig. S10). However, the anode with CNT/SiNPs/AC or CNT/SiNPs can only supply a capacity of 657.9 mAh/g and 515.3 mAh/g at 0.5 A/g after 200 cycles, respectively. The results indicate that the structure of the inner CNT and the outer SiC, which sandwich the SiNPs, is crucial for the fabrication of a Si-based anode with optimal performance. The high Young's modulus of SiC enables the effective dissipation of the strong stress caused by the volume expansion of Si, thus maintaining the integrity of the CNT/SiNPs/SiC. For comparison, it can be seen from Fig. S12 that the CNT/SiNPs and CNT/SiNPs/AC structures are susceptible to structural damage under strong stress.

The active phase for Li^+ storage of the CNT/SiNPs/SiC was evaluated by cyclic CV. As illustrated in Fig. 4b, the peaks observed at 0.18 V in the cathodic scan region can be attributed to the lithiation of crystalline Si into the amorphous Li_xSi alloys (a-Li_xSi). In the anodic scan region, two peaks at approximately 0.32 and 0.53 V can be attributed to the dealloying reaction of a-Li_xSi [40]. The voltage profiles of CNT/SiNPs/SiC at 2nd, 50th, 100th, 200th cycle demonstrate a smooth progression, with a reduction in polarization as the cycle progresses (Fig. 4c). This indicates the good electrochemical stability of the material. The rate performance of the samples was evaluated by discharge curves at current densities spanning from 0.2 to 4.0 A/g (Fig. 4d). In comparison to the CNT/SiNPs and CNT/SiNPs/AC, the CNT/SiNPs/SiC exhibits the most favourable rate performance, with discharge capacities of 1245.2, 1226.4, 1190.2,

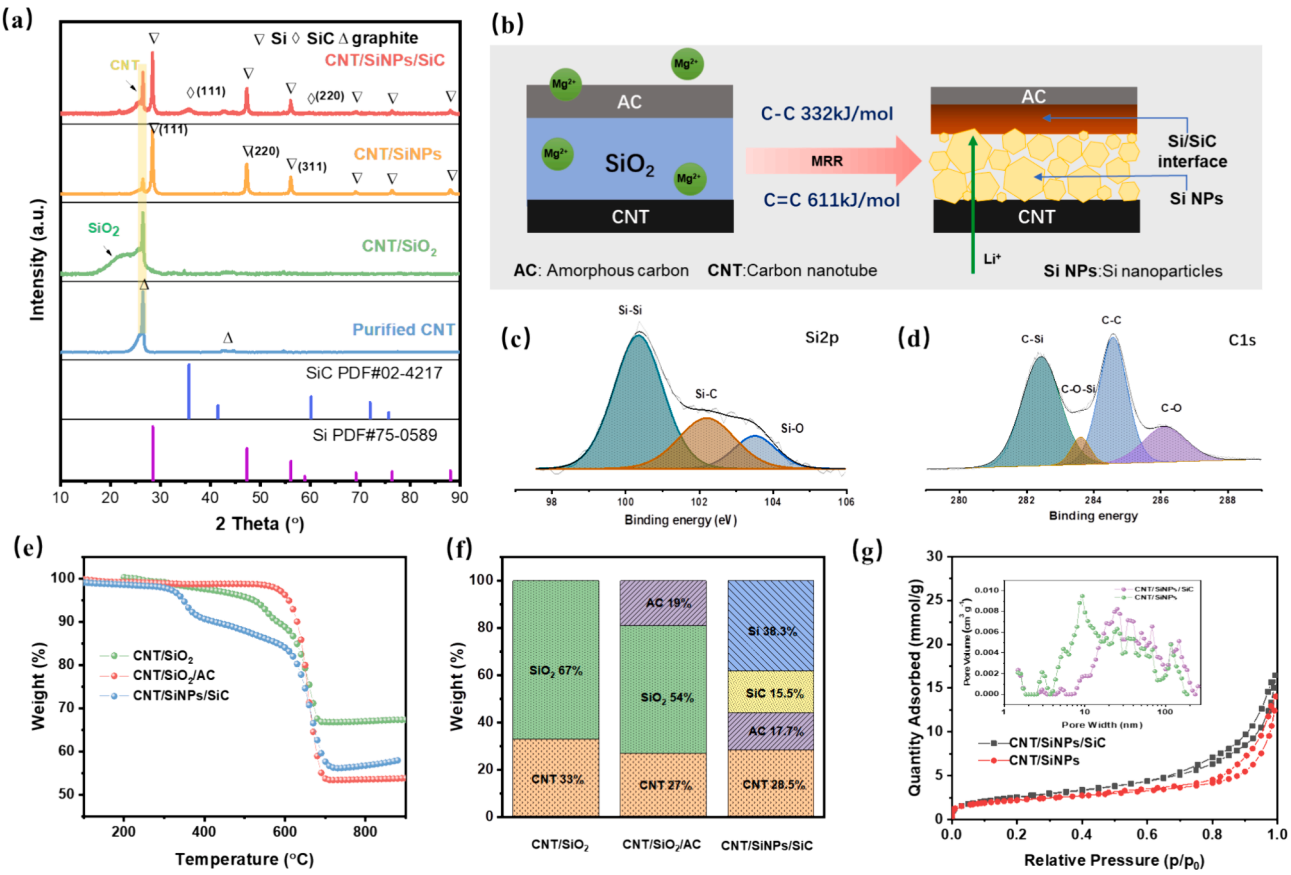

Fig. 3. (a) XRD patterns of samples. (b) Schematic diagram of CNT/SiNPs/SiC interface and spatial pore structure evolution. (c) and (d) XPS survey spectra, Si 2p, and C1s of CNT/SiNPs/SiC. (e) TG curves of samples and (f) phase ratio histogram of samples. (g) Nitrogen adsorption/desorption isotherms, the inset is pore size distribution curves of CNT/SiNPs and CNT/SiNPs/SiC.

1112.8, and 989.4 mAh/g at 0.2, 0.5, 1.0, 2.0, and 4.0 A/g, respectively (Fig S13). Upon re-establishing the current density to 0.2 A/g, the discharge capacity is observed to return to 1220.0 mAh/g. The CNT/SiNPs/SiC also exhibits a superior lifetime at a large current of 4.0 A/g, which possesses a high reversible capacity of 745.5 mAh/g and a capacity retention of 85.5 % even after 1000 cycles (Fig. 4e).

The results of the rate performance and cycling stability tests further confirm the structural and compositional advantages of CNT/SiNPs/SiC. In the CNT/SiNPs/SiC anode, CNT acts as a stress-buffering coach and electronic conductor, the stiff SiC inhibits the volumetric stress, and the most outer residual amorphous carbon layers can enhance the conductivity of the electrode. To ascertain the commercial viability of the CNT/SiNPs/SiC anode, a full cell comprising LFP as cathode was constructed. The cell exhibited an initially reversible capacity of 131.0 mAh/g at 2.0C, a capacity retention of 85.0 %, and maintained a working potential of approximately 3.3 V after 100cycles (Fig. S14). Furthermore, the full cell functions smoothly at rate tests ranging from 0.5C to 4.0C (Fig. S15). In comparison to the Si-based LIBs previously reported in the literature [41–43], the full cell assembled by the CNT/SiNPs/SiC anode exhibits superior performance (Fig. S16).

The lithium-ion diffusion kinetics of materials was investigated by EIS and GITT. The EIS of the CNT/SiNPs/SiC electrode is presented in Fig. 4f. Prior to the charge–discharge cycle, the EIS is composed of a semicircle in the high-frequency range, which represents the charge transfer resistance (R_{ct}), and a straight line in the low-frequency range, which reflects the diffusion resistance (W_o). Following the completion of the cycles, a new loop was observed in the middle frequency region, which is indicative of the formation of the SEI. The equivalent circuits employed to fit the EIS data, the values and errors of the electric components are shown in Fig. 4g and Tab. S3. The R_{ct} value before the cycle is 73.8 Ω cm^2 and increases to 87.6 Ω cm^2 at the first cycle, which can be attributed to the large polarization effect at the first discharge. However, following the initial cycle, the R_{ct} value exhibits a marked decline as the cycling progresses, reaching a value of 42.8 Ω cm^2 after 100 cycles. This trend was replicated in the parallel test group (Fig. 4h). The inner CNTs in the CNT/SiNPs/SiC act as an electronic conductor, thus facilitating the transfer of charges during electrode reactions. The outer, rigid SiC further inhibits volumetric stress, preventing damage to the CNT and thus maintaining the conductive network. Furthermore, the porous structure of CNT/SiNPs/SiC necessitates a relatively lengthy wetting process, which also results in a reduction of the Rct value with cycles. Conversely, the R_{ct} of CNT/SiNPs/AC exhibits a marked increase after 100 cycles (Fig. S17), thereby corroborating the pivotal role of the stiff SiC in preventing the cracking of the outer carbonaceous layers during the cycling process. The interfacial resistance (R_f) is indicative of the blockage of ion and electron transport at the electrode–electrolyte interface, as described by reference [44]. The R_f value of the CNT/SiNPs/SiC electrode decreases gradually with the number of cycles, indicating that the SEI tends to stabilise rather than undergo repeated formation, which would otherwise result in higher ions and electrons resistance.

Li^+ transport kinetics in the Si based electrodes was further studied through GITT and the results are shown in Fig. S18. On the basis of GITT curves of CNT/SiNPs/AC and CNT/SiNPs/SiC electrodes after 100 cycles (Fig. S18a), the diffusion coefficient of Li^+ (D_{Li+}) was calculated according to the following equation and then the curves of log D_{Li+} vs lithiation state of Si was plotted as shown by Fig. S18b.

$$D_{Li+} = \frac{4L^2}{\pi\tau}\left(\frac{\Delta E_S}{\Delta E_\tau}\right)^2$$

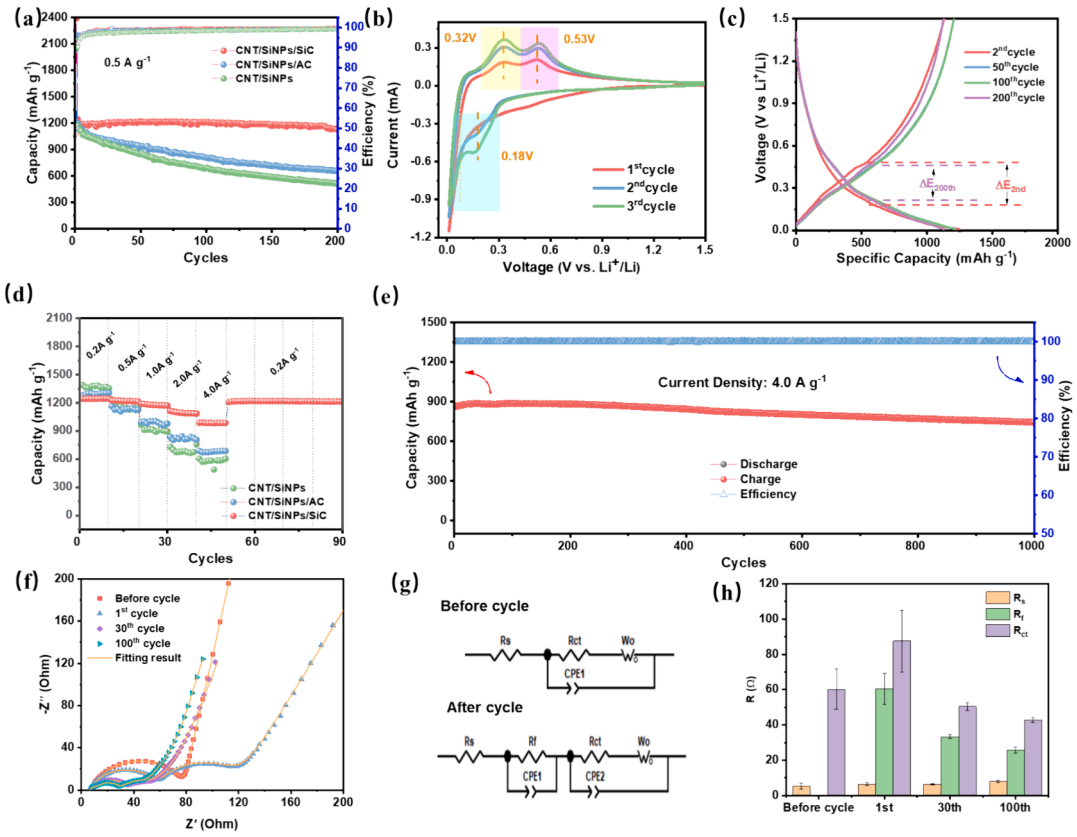

Fig. 4. (a) Cycling-induced variation of discharge capacity and CE for CNT/SiNPs, CNT/SiNPs/AC and CNT/SiNPs/SiC at 0.5A/g for 200 cycles. (b) CV curves of CNT/SiNPs/SiC at 0.2 mV s^{-1}. (c) Voltage profiles of CNT/SiNPs/SiC at 0.5 A/g. (d) Rate capability of CNT/SiNPs, CNT/SiNPs/AC and CNT/SiNPs/SiC at current density of from 0.2 to 4.0 A/g. (e) Cycling performance of CNT/SiNPs/SiC at 4.0 A/g for 1000 cycles. (f) Nyquist plots and EIS fitting results of the CNT/SiNPs/SiC electrode before and after cycles and (g) Equivalent circuits. (h) Mean and standard deviation of three EIS tests performed on the electrodes.

where L refers to the diffusion length of Li^+ (equal to the electrode thickness), stands for the relaxation time (s), ΔE_s represents the steady-state potential change via the current pulse, and ΔE_τ is the potential change in current pulse after subtracting the iR drop. By comparing the diffusion curves of samples, the faster Li^+ diffusion rate of the cycled CNT/SiNPs/SiC reflects the good electrochemical kinetics.

The morphology of the electrodes was examined before and after the cycling process in order to assess the stability of the samples (Fig. 5a–f). After 200 cycles, there were no discernible changes in the topography and cross-sectional surface of the electrode with CNT/SiNPs/SiC, with an increase in electrode thickness of 17 % (As illustrated in Fig. S19, the electrode thickness from average 12.0 to 14.0 μm). In contrast, numerous large cracks were produced after 200 cycles in the case of electrodes with CNT/SiNPs/AC or CNT/SiNPs (Fig. S20 and Fig. S21). Furthermore, the electrodes with CNT/SiNPs/AC exhibited volumetric expansion, reaching approximately 50 % (Fig. S22 and Fig. S23). The results indicate that the inner CNT and the outer SiC play a crucial role in stabilising the electrode structure.

The microstructure of the samples following the completion of the cycles was examined by TEM in order to evaluate the situation of the SiNPs. The results of this examination are shown in Fig. 5g and h. It can be observed that some of the SiNPs have separated from the CNT/SiNPs/AC. The separated SiNPs have lost their conductive pathways and will gradually evolve into what is known as “dead silicon” in the subsequent cycles. In contrast, the interface structure of CNT/SiNPs/SiC remains stable, with the SiNPs effectively encapsulated between the CNT and SiC due to the limited stress imposed by the stiff SiC. The surface displacements of the samples were simulated by FEM using the C//Si//C and C//Si//SiC models (Fig. S24). The smaller surface displacement of C//Si//SiC (18.2 nm) relative to C//Si//C (27.1 nm) can be attributed to the limitation of Si volume expansion by the rigid SiC, as well as the effective absorption of in-plane shear energy by the inner CNT and outer SiC architecture (Fig. 5i). In the CNT/SiNPs/SiC anode, the SiNPs are able to avoid self-cracks due to their nano-scale dimensions. Furthermore, the sandwiched structure of CNT and SiC, which act as interfaces between SiNPs, can effectively buffer the volumetric effects and maintain the integrity of CNT/SiNPs/SiC during the (de)lithiation process. The inner CNT can act as a conductor to facilitate the transfer of electrons and a buffer to mitigate the volumetric stress induced by Si lithiation. The outer stiff SiC interfaced with SiNPs can inhibit the substantial structure inflation, thereby ensuring the structural stability of CNT/SiNPs/SiC and consequently the excellent cycling and rate performance [45,46].

The composition and structure of the SEI film are also crucial factors in determining the cycling stability of the electrode [47]. Although SEI film can facilitate Li^+ transfer, the repeated reconfiguration of SEI film can deplete the electrolyte and increase the Li^+ diffusion distance, thereby slowing the electrode reaction kinetics. The stress management capabilities of the sandwich heterostructure of CNT/SiNPs/SiC can significantly reduce the reorganization of the SEI film. Furthermore, the composition of the SEI film can be optimised by the additives, which has been demonstrated to be an effective strategy for improving the electrochemical performance of electrodes. FEC as a fluorinated derivative of EC, is one of the most commonly used electrolyte additives for Si-based anodes. As an additive, FEC can be reduced into polymerised vinyl carbonate (poly (VC)) and LiF, which modify the SEI film. It has been demonstrated that the introduction of FEC molecules into the inner Helmholtz plane (IHP) can stabilise the SEI film of Si-based anodes. Firstly, the adsorption of the FEC molecules on Si and SiC surfaces was calculated using DFT, taking into account the parallel orientation of the FEC molecules on the plates of the Si (1 1 1) and SiC (1 1 1) surfaces

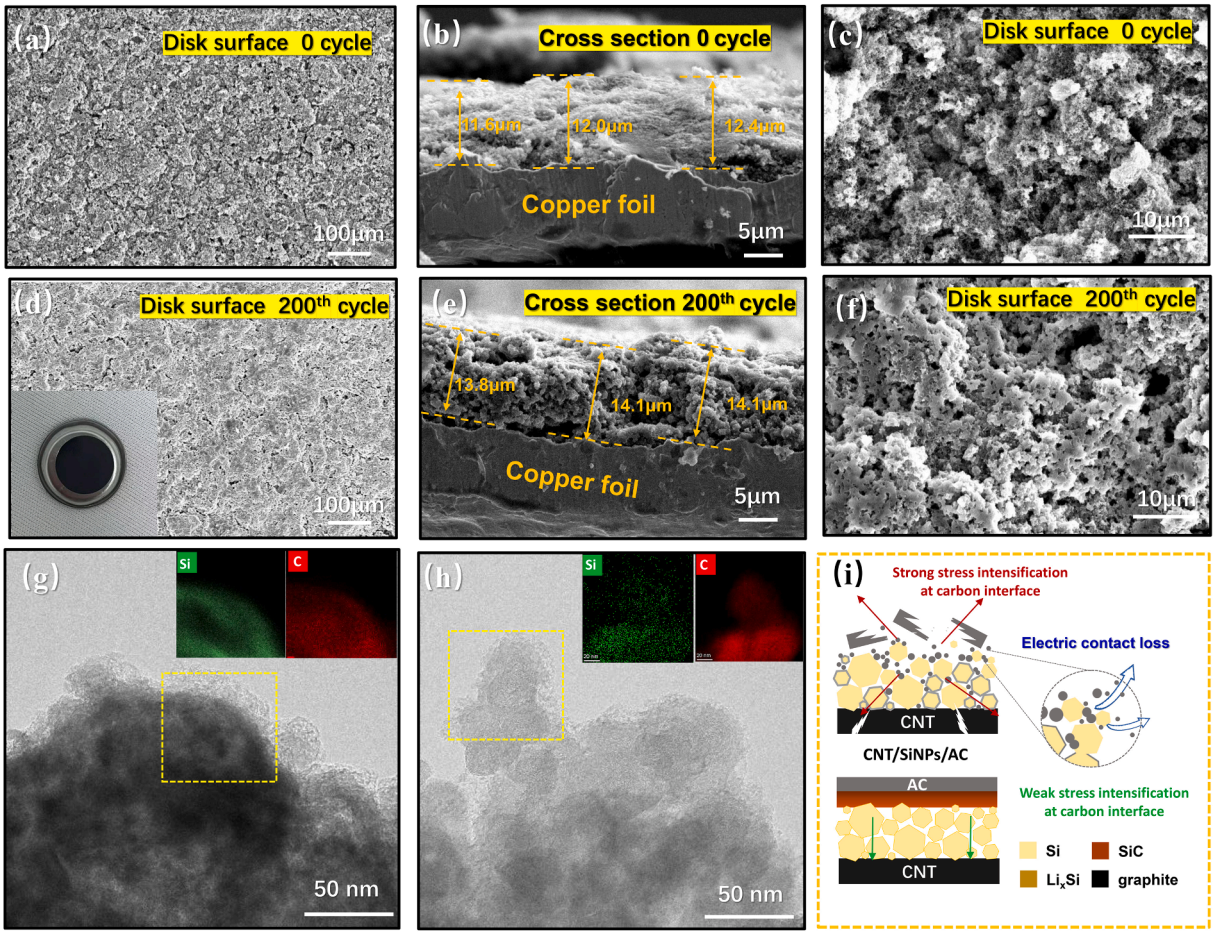

Fig. 5. SEM images of (a, d) surface, (b, e) cross-sectional surface and (c, f) dispersed samples by deionized water of CNT/SiNPs/SiC electrode before and after 200 cycles. TEM of (g) CNT/SiNPs/SiC and (h) CNT/SiNPs/AC electrode after 200 cycles, the inset is corresponding element mapping of Si and C in samples. (i) Schematic diagram of dead silicon formation in CNT/SiNPs/AC during cycles.

(Fig. 6a and b). It is evident that the binding energies of SiC (1 1 1) to FEC (−4.3 eV) are considerably more negative than those of Si (−0.4 eV), indicating a markedly stronger adsorption capacity. This may result in the formation of an FEC-rich IHP at the SiC interface [48].

XPS was performed to detect the chemical composition of SEI formed onto the electrode. In the cycled CNT/SiNPs/SiC, the major elements are O (42.91 at%) and C (34.31 at%), along with a low concentration of F and P (Fig. 6c). From the F 1s spectrum, LiF and LixPFy are the major species derived from $LiPF_6$. The content of Li_xPFy in CNT/SiNPs/SiC is less than that observed in both CNT/SiNPs and CNT/SiNPs/AC, indicating that the decomposition and recombination of the electrolyte around CNT/SiNPs/SiC are inhibited (Fig. 6d–f). In the C 1s spectrum, the peaks at 284.8, 286.3, 288.4 and 289.8 eV correspond to the C—C, C—O, C═O and carbonate-containing species, respectively [49]. The ratio of carbonate-containing species (labelled as $LixCO_3$) in the CNT/SiNPs is greater than in the other two samples, indicating that it underwent an excessive electrochemical reduction and consumption of electrolyte without any outer protective layer around Si. Furthermore, the presence of Si-Li bonds in the Si 2p spectra of CNT/SiNPs indicates the occurrence of irreversible lithiation side reactions at the electrolyte interface of the sample. Consequently, the presence of Si-Si bonds in CNT/SiNPs/SiC indicates the reversibility of good Li^+ intercalation of the sample. Although the amorphous carbon layers of CNT/SiNPs/AC can prevent the direct interaction of Si from the electrolyte, thereby reducing the consumption of electrolyte, the large volumetric stress of Si lithiation can cause the amorphous carbon layers to break, thereby losing their protective effect. Consequently, the Si 2p spectrum of CNT/SiNPs/AC exhibits a weak Si elemental excitation signal. The introduction of a rigid SiC layer between the Si and CNT can prevent the stress caused by Si lithiation, thereby reducing the degradation of the amorphous carbon layers. Consequently, the SEI around the CNT/SiNPs/SiC exhibits excellent stability. Combining the Si 2p with the O1s spectrum, a series of additional peak assignments such as siloxane structures (R—O—C—O—R') can be discerned, which correlates with the preferential adsorption of FEC on the SiC surface. The organics-dominated SEI owns the better conductivity, it could facilitate the electrons transfer in CNT/SiNPs/SiC [17].

4. Conclusions

A novel sandwich material of CNT/SiNPs/SiC that Si nanoparticles (SiNPs) encapsuled between carbon nanotube (CNT) and silicon carbide (SiC) has been fabricated. The outer SiC/Si interface inhibits the volume changes due to the rigid SiC. The inner CNT/Si interface buffers the stress resulted by the volume change of Si during (de)lithiation and plays as a conductor to enhance electrons transfer owing to the high elastic modulus and good conductivity of CNT. Furthermore, the theoretical calculations and experimental results consistently show that the SiC (1 1 1) surface of Si/SiC interface can enhance the adsorption of the FEC molecules on CNT/SiNPs/SiC to stabilize the SEI. Therefore, as the anode materials of LIBs, the CNT/SiNPs/SiC anode exhibits an excellent stability and rate performance. It can output a capacity of 1127.2 mAh/g at 0.5 A/g with a retention rate of 95.6 % after 200 cycles and a capability of 745.5 mAh/g at 4.0 A/g after 1000 cycles. Compared with

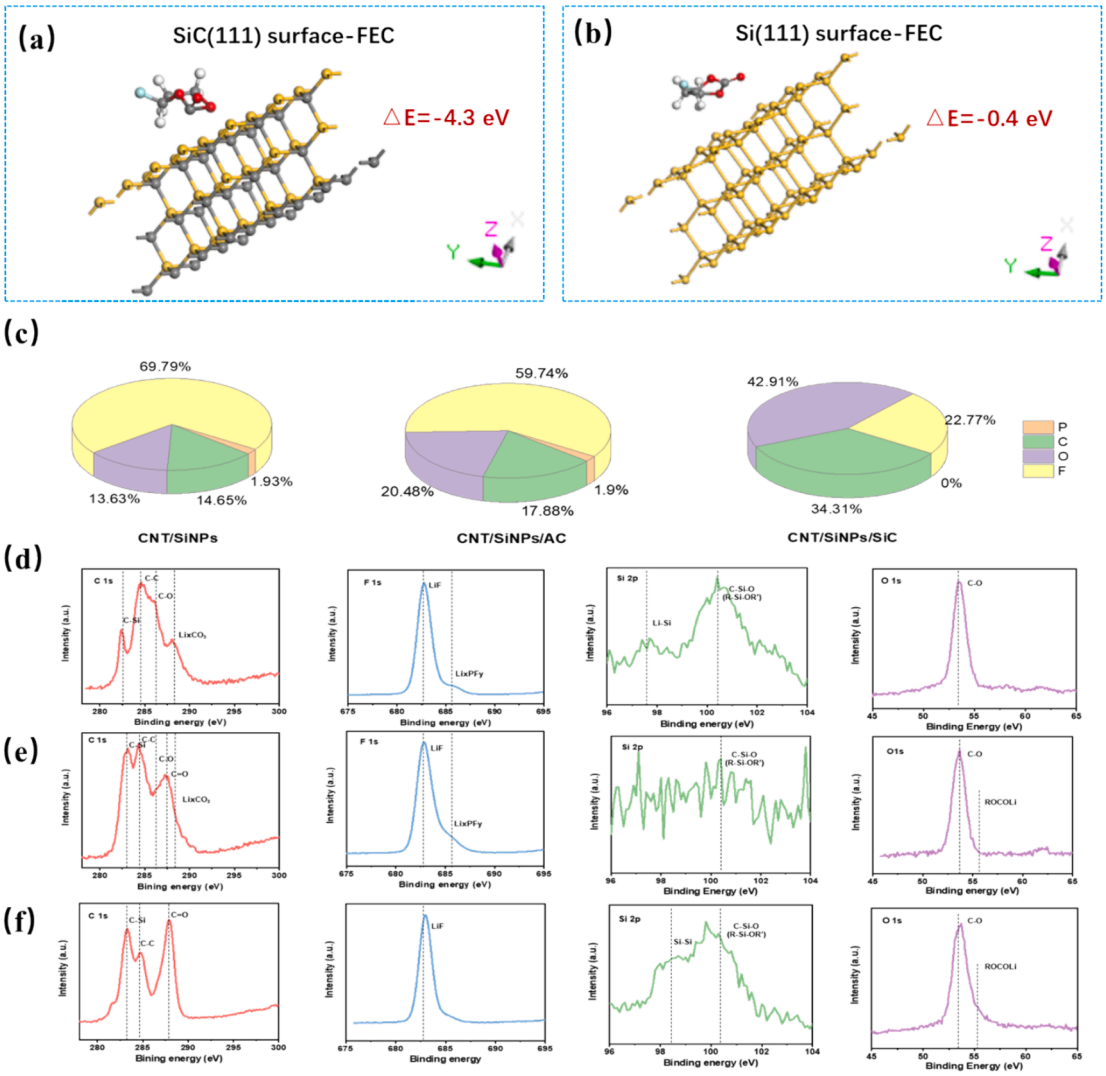

Fig. 6. Main views of the configuration after adsorbing FEC on (a) SiC (1 1 1) and (b) Si (1 1 1) surface. The chemical composition of electrode surface after 10 cycles, (c) interfacial atom concentrations of cycled CNT/SiNPs, CNT/SiNPs/AC, and CNT/SiNPs/SiC. C 1s, F1s, Si 2p and O 1s XPS spectra of cycled (d) CNT/SiNPs, (e) CNT/SiNPs/AC, and (f) CNT/SiNPs/SiC.

previously reported homogeneous interface modification by using materials of carbon or SiC, the dual-interface sandwiched Si anode exhibits the better cycling stability and rate performance.

CRediT authorship contribution statement

Fang Di: Writing – original draft, Conceptualization. **Xin Gu:** Data curation. **Yang Chu:** Investigation. **Lixiang Li:** Conceptualization. **Xin Geng:** Data curation. **Chengguo Sun:** Methodology. **Weimin Zhou:** Formal analysis. **Han Zhang:** Methodology. **Hongwei Zhao:** Methodology. **Lin Tao:** Software. **Guangshen Jiang:** Methodology. **Xueyuan Zhang:** Project administration. **Baigang An:** Conceptualization.

Declaration of competing interest

The authors declare that they have no known competing financial interests or personal relationships that could have appeared to influence the work reported in this paper.

Data availability

Data will be made available on request.

Acknowledgments

Financial supports by the Natural Science Foundation of China (NSFC) No. 52371224, 51972156, 51672117, 51672118, The specific research fund of the Innovation Platform for Academicians of Hainan Province (YSPTZX202315) and Distinguished Professor of Liaoning Province (2017) are acknowledged.

Appendix A. Supplementary material

Supplementary material to this article can be found online at https://doi.org/10.1016/j.jcis.2024.05.081.

References

[1] J. Sung, N. Kim, J. Ma, J.H. Lee, S.H. Joo, T. Lee, S. Chae, M. Yoon, Y. Lee, J. Hwang, S.K. Kwak, J. Cho, Subnano-sized silicon anode via crystal growth inhibition mechanism and its application in a prototype battery pack, Nat. Energy 6 (2021) 1164–1175, https://doi.org/10.1038/s41560-021-00945-z.
[2] C.H. Yu, X. Chen, Z.X. Xiao, C. Lei, C.X. Zhang, X.Q. Lin, B.Y. Shen, R.F. Zhang, F. Wei, Highly porous carbon-coated silicon nanoparticles with canyon-like surfaces as a high-performance anode material for Li-ion batteries, Nano Lett. 19 (2019) 5124–5132, https://doi.org/10.1039/C7TA10093K.
[3] H. Zhang, Y. Zhang, L. Li, H. Zhou, M. Wang, L. Li, X. Geng, B. An, C. Sun, A rational design of titanium-based heterostructures as electrocatalyst for boosted

conversion kinetics of polysulfides in Li-S batteries, J. Colloid Interface Sci. 633 (2023) 432–440, https://doi.org/10.1016/j.jcis.2022.11.092.
[4] C.Z. Zhang, F. Wang, J. Han, S. Bai, J. Tan, J.S. Liu, F. Li, Challenges and recent progress on silicon-based anode materials for next-generation lithium-ion batteries, Small Struct. 2 (2021) 19, https://doi.org/10.1002/sstr.202100009.
[5] C. Zhou, X. Gong, Y. Feng, J. Lu, Y. Fu, Z. Wang, J. Liu, Constructing an artificial boundary to regulate solid electrolyte interface formation and synergistically enhance stability of nano-Si anodes, J. Colloid Interface Sci. 619 (2022) 158–167, https://doi.org/10.1016/j.jcis.2022.03.111.
[6] J. Xie, L. Tong, L.W. Su, Y.W. Xu, L.B. Wang, Y.H. Wang, Core-shell yolk-shell Si@C@Void@C nanohybrids as advanced lithium-ion battery anodes with good electronic conductivity and corrosion resistance, J. Power Sources 342 (2017) 529–536, https://doi.org/10.1016/j.jpowsour.2016.12.094.
[7] J. Zhao, K. Yang, J. Wang, D. Wei, Z. Liu, S. Zhang, W. Ye, C. Zhang, Z. Wang, X. Yang, Expired milk powder emulsion-derived carbonaceous framework/Si composite as efficient anode for lithium-ion batteries, J. Colloid Interface Sci. 638 (2023) 99–108, https://doi.org/10.1016/j.jcis.2023.01.106.
[8] R.P. Liu, C. Shen, Y. Dong, J.L. Qin, Q. Wang, J. Iocozzia, S.Q. Zhao, K.J. Yuan, C. P. Han, B. Lin, Sandwich-like CNTs/Si/C nanotubes as high-performance anode materials for lithium-ion batteries, J. Mater. Chem. A 6 (2018) 14797–14804, https://doi.org/10.1039/c8ta04686g.
[9] S. Wu, F. Di, J. Zheng, H. Zhao, H. Zhang, L.X. Li, X. Geng, C. Sun, H. Yang, W. M. Zhou, D. Ju, B. An, Self-healing polymer binders for the Si and Si/carbon anodes of lithium-ion batteries, New Carbon Mater. 37 (2022) 802–826, https://doi.org/10.1016/S1872-5805(22)60638-3.
[10] Z. Qi, L. Dai, Z. Wang, L. Xie, J. Chen, J. Cheng, G. Song, X. Li, G. Sun, C. Chen, Optimizing the carbon coating to eliminate electrochemical interface polarization in a high performance silicon anode for use in a lithium-ion battery, New Carbon Mater. 37 (2022) 245–258, https://doi.org/10.1016/S1872-5805(22)60580-8.
[11] J.J. Lu, J.H. Liu, X.Z. Gong, S. Pang, C.Y. Zhou, H.X. Li, G.Y. Qian, Z. Wang, Upcycling of photovoltaic silicon waste into ultrahigh areal-loaded silicon nanowire electrodes through electrothermal shock, Energy Storage Mater. 46 (2022) 594–604, https://doi.org/10.1016/j.ensm.2022.01.051.
[12] F. Di, Z. Wang, C. Ge, L. Li, X. Geng, C. Sun, H. Yang, W. Zhou, D. Ju, B. An, F. Li, Hierarchical pomegranate-structure design enables stress management for volume release of Si anode, J. Mater. Sci. Technol. 157 (2023) 1–10, https://doi.org/10.1016/j.jmst.2023.02.014.
[13] Z. Yang, Y. Ding, Y. Jiang, P. Zhang, H. Jin, Hierarchical C/SiO_x/TiO_2 ultrathin nanobelts as anode materials for advanced lithium ion batteries, Nanotechnology 29 (2018) 405602, https://doi.org/10.1088/1361-6528/aad2f9.
[14] Y. Hu, R. Demir-Cakan, M. Titirici, J. Muller, R. Schlogl, M. Antonietti, J. Maier, Superior storage performance of a Si@SiO_x/C nanocomposite as anode material for lithium-ion batteries, Angew. Chem. Int. Ed. 47 (2008) 1645–1649, https://doi.org/10.1002/anie.200704287.
[15] L. Zhang, C. Wang, Y. Dou, N. Cheng, D. Cui, Y. Du, P. Liu, M. Mamun, S. Zhang, H. Zhao, A yolk-shell structured silicon anode with superior conductivity and high tap density for full lithium-ion batteries, Angew. Chem. Int. Ed. 58 (2019) 8824–8828, https://doi.org/10.1002/anie.201903709.
[16] X. Huang, X. Sui, H. Yang, R. Ren, Y. Wu, X. Guo, J. Chen, HF-free synthesis of Si/C yolk/shell anodes for lithium-ion batteries, J. Mater. Chem. A 6 (2018) 2593–2599, https://doi.org/10.1039/C7TA08283E.
[17] X. Zhang, D. Wang, X. Qiu, Y. Ma, D. Kong, K. Müllen, X. Li, L. Zhi, Stable high-capacity and high-rate silicon-based lithium battery anodes upon two-dimensional covalent encapsulation, Nat. Commun. 11 (2020) 3826, https://doi.org/10.1038/s41467-020-17686-4.
[18] J. Ryu, T. Chen, T. Bok, G. Song, J. Ma, C. Hwang, L. Luo, H. Song, J. Cho, C. Wang, S. Zhang, S. Park, Nat. Commun. 9 (2018) 2924, https://doi.org/10.1038/s41467-018-05398-9.
[19] J. Sung, J. Ma, S.H. Choi, J. Hong, N. Kim, S. Chae, Y. Son, S.Y. Kim, J. Cho, Mechanical mismatch-driven rippling in carbon-coated silicon sheets for stress-resilient battery anodes, Adv. Mater. 31 (2019) 1900970, https://doi.org/10.1002/adma.201900970.
[20] S. Park, J. Sung, S. Chae, J. Hong, T. Lee, Y. Lee, H. Cha, S.Y. Kim, J. Cho, Scalable synthesis of hollow β-SiC/Si anodes via selective thermal oxidation for lithium-ion batteries, ACS Nano 14 (2020) 11548–11557, https://doi.org/10.1021/acsnano.0c04013.
[21] L. Shen, C. Xu, J. Gao, J. Tao, Q. Zhang, Y. Chen, Y. Lin, Z. Huang, J. Li, Scalable synthesized high-performance TiO_2-Si-C hybrid anode for lithium batteries, J. Energy Chem. 77 (2023) 348–358, https://doi.org/10.1016/j.jechem.2022.10.044.
[22] K. Ogata, S. Jeon, D. Ko, I.S. Jung, J.H. Kim, K. Ito, Y. Kubo, K. Takei, S. Saito, Y. Cho, H. Park, J. Jang, H. Kim, J. Kim, Y.S. Kim, W. Choi, M. Koh, K. Uosaki, S. G. Doo, Y. Hwang, S. Han, Evolving affinity between Coulombic reversibility and hysteretic phase transformations in nanostructured silicon-based lithium-ion batteries, Nat. Commun. 9 (2018) 479, https://doi.org/10.1021/am500066j.
[23] Y. He, L. Jiang, T. Chen, Y. Xu, H. Ji, R. Yi, D. Xue, M. Song, A. Genc, C. Marquis, L. Pullan, T. Tessner, Progressive growth of the solid-electrolyte interphase towards the Si anode interior causes capacity fading, Nat. Nanotechnol. 16 (2021) 1113–1120, https://doi.org/10.1038/s41565-021-00947-8.
[24] Y. Zhou, M. Su, X. Yu, Y. Zhang, J.G. Wang, X. Ren, R. Cao, W. Xu, D.R. Baer, Y. Du, Real-time mass spectrometric characterization of the solid-electrolyte interphase of a lithium-ion battery, Nat. Nanotechnol. 15 (2020) 224–230, https://doi.org/10.1038/s41565-019-0618-4.
[25] A.L. Michan, B.S. Parimalam, M. Leskes, R.N. Kerber, T. Yoon, C.P. Grey, B. L. Lucht, Fluoroethylene carbonate and vinylene carbonate reduction: understanding lithium-ion battery electrolyte additives and solid electrolyte interphase formation, Chem. Mater. 28 (2016) 8149–8159, https://doi.org/10.1021/acs.chemmater.6b02282.
[26] J. Wang Z. Yang B. Mao Y. Wang Y. Jiang M. Cao Transgenic Engineering on Silicon Surfaces Enables Robust Interface Chemistry 7 2022 2781 2791 10.1021/acsenergylett.2c01202.
[27] W. Luo, Y. Wang, S. Chou, Y. Xu, W. Li, B. Kong, S.X. Dou, H.K. Liu, J. Yang, Critical thickness of phenolic resin-based carbon interfacial layer for improving long cycling stability of silicon nanoparticle anodes, Nano Energy 27 (2016) 255–264, https://doi.org/10.1016/j.nanoen.2016.07.006.
[28] Y.F. Zhang, Y.J. Li, Z.Y. Wang, K.J. Zhao, Lithiation of SiO_2 in Li-ion batteries: in situ transmission electron microscopy experiments and theoretical studies, Nano Lett. 14 (2014) 7161–7170, https://doi.org/10.1021/nl503776u.
[29] Y.S. Choi, M. Pharr, K.H. Oh, J.J. Vlassak, A simple technique for measuring the fracture energy of lithiated thin-film silicon electrodes at various lithium concentrations, J. Power Sources 294 (2015) 159–166, https://doi.org/10.1016/j.jpowsour.2015.06.063.
[30] T. Lee, N. Kim, J. Lee, Y. Lee, J. Sung, H. Kim, S. Chae, H. Cha, Y. Son, S.K. Kwak, J. Cho, Suppressing deformation of silicon anodes via interfacial synthesis for fast-charging lithium-ion batteries, Adv. Energy Mater. 13 (2023) 2301139, https://doi.org/10.1002/aenm.202301139.
[31] X.H. Liu, J.Y. Huang, In situ TEM electrochemistry of anode materials in lithium ion batteries, Energy Environ. Sci. 4 (2011) 3844–3860, https://doi.org/10.1039/C1EE01918J.
[32] F. Xi, Z. Zhang, X. Wan, S. Li, W. Ma, X. Chen, R. Chen, B. Luo, L. Wang, High-performance porous silicon/nano silver anodes from industrial low-grade silicon for lithium-ion batteries, ACS Appl. Mater. Interfaces 12 (2020) 49080–49089, https://doi.org/10.1021/acsami.0c14157.
[33] J. Liu, P. Kopold, P.A. van Aken, J. Maier, Y. Yu, Energy storage materials from nature through nanotechnology: a sustainable route from reed plants to a silicon anode for lithium-ion batteries, Angew. Chem. 127 (2015) 9768–9772, https://doi.org/10.1002/ange.201503150.
[34] N. Kim, H. Park, N. Yoon, J. Lee, Zeolite-templated mesoporous silicon particles for advanced lithium-ion battery anodes, ACS Nano 12 (2018) 3853–3864, https://doi.org/10.1021/acsnano.8b01129.
[35] M. Dasog, L.F. Smith, T.K. Purkait, J. Veinot, Low temperature synthesis of silicon carbide nanomaterials using a solid-state method, Chem. Commun. 49 (2013) 7004–7006, https://doi.org/10.1039/c3cc43625j.
[36] X.Y. Liu, H.W. Zhao, S. Jiang, S. Wu, T. Zhao, L.X. Li, X. Geng, H.M. Yang, W. M. Zhou, C.G. Sun, Y.Q. Chen, B.G. An, A porous SiC/C composite material constructed by the ordered mesoporous SiC interfacing with the ordered mesoporous carbon and its supercapacitor performance, J. Alloy. Compd. 881 (2021) 160442–160450, https://doi.org/10.1016/j.jallcom.2021.160442.
[37] M. Dasog, C. Rachinsky, J. Veinot, From Si and C encapsulated SiO_2 to SiC: exploring the influence of sol-gel polymer substitution on thermally induced nanocrystal formation, J. Mater. Chem. 21 (2011) 12422–12427, https://doi.org/10.1039/c1jm11858g.
[38] H. Dong, X. Fu, J. Wang, P. Wang, H. Ding, R. Song, S. Wang, R. Li, S. Li, In-situ construction of porous Si@C composites with LiCl template to provide silicon anode expansion buffer, Carbon 173 (2021) 687–695, https://doi.org/10.1016/j.carbon.2020.11.042.
[39] H. Zhao, L. Li, Y. Liu, X. Geng, H. Yang, C. Sun, B. An, Synthesis and ORR performance of nitrogen-doped ordered microporous carbon by CVD of acetonitrile vapor using silanized zeolite as template, Appl. Surf. Sci. 504 (2020) 144438, https://doi.org/10.1016/j.apsusc.2019.144438.
[40] X. Fan, T. Cai, S. Wang, Z. Yang, W. Zhang, Carbon nanotube-reinforced dual carbon stress-buffering for highly stable silicon anode material in lithium-ion battery, Small 19 (2023) 2300431, https://doi.org/10.1002/smll.202300431.
[41] T.S. Mu, S.F. Lou, N.G. Holmes, C.H. Wang, M.X. He, B.C. Shen, X.T. Lin, P.J. Zuo, Y.L. Ma, R.Y. Li, C.Y. Du, J.J. Wang, G.P. Yin, X.L. Sun, Reversible silicon anodes with long cycles by multifunctional volumetric buffer layers, ACS Appl. Mater. Interfaces 13 (2021) 4093–4101, https://doi.org/10.1021/acsami.0c21455.
[42] Z. Yi, N. Lin, Y.Y. Zhao, W.W. Wang, Y. Qian, Y.C. Zhu, Y.T. Qian, A flexible micro/nanostructured Si microsphere cross-linked by highly-elastic carbon nanotubes toward enhanced lithium-ion battery anodes, Energy Storage Mater. 17 (2019) 93–100, https://doi.org/10.1016/j.ensm.2018.07.025.
[43] Q. Wang, T. Meng, Y. Li, J. Yang, B. Huang, S. Ou, C. Meng, S. Zhang, Y. Tong, Consecutive chemical bonds reconstructing surface structure of silicon anode for high-performance lithium-ion battery, Energy Storage Mater. 39 (2021) 354–364, https://doi.org/10.1016/j.ensm.2021.04.043.
[44] B. Philippe, R. Dedryvere, J. Allouche, F. Lindgren, M. Gorgoi, H. Rensmo, D. Gonbeau, K. Edstrom, Nanosilicon electrodes for lithium-ion batteries: interfacial mechanisms studied by hard and soft X-ray photoelectron spectroscopy, Chem. Mater. 24 (2012) 1107–1115, https://doi.org/10.1021/cm2034195.
[45] F. Di, N. Wang, L.X. Li, X. Geng, H.M. Yang, W.M. Zhou, C.G. Sun, B.G. An, Coral-like porous composite material of silicon and carbon synthesized by using diatomite as self-template and precursor with a good performance as anode of lithium-ions battery, J. Alloys Compd. 8 (2021) 854, https://doi.org/10.1016/j.jallcom.2020.157253.
[46] H.P. Jia, X.L. Li, J.H. Song, X. Zhang, L.L. Luo, Y. He, B.S. Li, Y. Cai, S.Y. Hu, X. C. Xiao, C.M. Wang, K.M. Rosso, R. Yi, R. Patel, J.G. Zhang, Hierarchical porous silicon structures with extraordinary mechanical strength as high-performance lithium-ion battery anodes, Nat. Commun. 11 (2020) 1474, https://doi.org/10.1038/s41467-020-15217-9.
[47] H. Li, L. Li, J. Zheng, H. Huang, H. Zhang, B. An, X. Geng, C. Sun, Thermal decomposition assisted construction of Nano-Li_3N sites interface layer enabling

homogeneous Li deposition, ChemSusChem (2023) e202202220, https://doi.org/10.1002/cssc.202202220.
[48] L. Tao, D. Dastan, W. Wang, P. Poldorn, X. Meng, M. Wu, H. Zhao, H. Zhang, L. Li, B. An, Metal-decorated InN monolayer senses N_2 against CO_2, ACS Appl. Mater. Interfaces 15 (2023) 12534–12544, https://doi.org/10.1021/acsami.2c21463.
[49] W. Huang, J. Wang, M.R. Braun, Z. Zhang, Y. Li, D.T. Boyle, P.C. McIntyre, Y. Cui, Dynamic structure and chemistry of the silicon solid-electrolyte interphase visualized by cryogenic electron microscopy, Matter 1 (2019) 1232–1245, https://doi.org/10.1016/j.matt.2019.09.020.